

# Coexistence of magnetic order and valence fluctuations in a Kondo lattice system $\text{Ce}_2\text{Rh}_3\text{Sn}_5$ .

M. Gamża<sup>1,2,3</sup>, R. Gumeniuk<sup>2,4</sup>, U. Burkhardt<sup>2</sup>, W. Schnelle<sup>2</sup>, H. Rosner<sup>2</sup>, A. Leithe-Jasper<sup>2</sup>, and A. Ślebarski<sup>3,5</sup>

<sup>1</sup>*Jeremiah Horrocks Institute for Mathematics, Physics and Astrophysics,  
University of Central Lancashire, Preston PR1 2HE, UK*

<sup>2</sup>*Max-Planck Institute for Chemical Physics of Solids, D-01187 Dresden, Germany*

<sup>3</sup>*Institute of Physics, University of Silesia, 40-007 Katowice, Poland*

<sup>4</sup>*Institute of Experimental Physics, TU Bergakademie Freiberg, 09596 Freiberg, Germany and*

<sup>5</sup>*Centre for Advanced Materials and Smart Structures,  
Polish Academy of Sciences, 50-950 Wrocław, Poland*

(Dated: November 28, 2018)

We report on the electronic band structure, structural, magnetic and thermal properties of  $\text{Ce}_2\text{Rh}_3\text{Sn}_5$ . Ce  $L_{\text{III}}$ -edge XAS spectra give direct evidence for an intermediate valence behaviour. Thermodynamic measurements reveal magnetic transitions at  $T_{\text{N1}} \approx 2.9$  K and  $T_{\text{N2}} \approx 2.4$  K. Electrical resistivity shows behaviour typical for Kondo lattices. The coexistence of magnetic order and valence fluctuations in a Kondo lattice system we attribute to a peculiar crystal structure in which Ce ions occupy two distinct lattice sites. Analysis of the structural features of  $\text{Ce}_2\text{Rh}_3\text{Sn}_5$ , together with results of electronic band structure calculations and thermodynamic data indicate that Ce2 ions are in an intermediate valence state with the ground state electronic configuration close to  $4f^0$ , whereas Ce1 ions are trivalent ( $4f^1$ ) and contribute to the low temperature magnetic ordering. Thus, our joined experimental and theoretical investigations classify  $\text{Ce}_2\text{Rh}_3\text{Sn}_5$  as a multivalent charge-ordered system.

PACS numbers: 71.28.+d, 75.30.Mb, 71.27.+a, 79.60.-i, 71.20.Lp

Keywords: Kondo lattice, intermediate valence, mixed valence, electronic structure, magnetic, thermal and transport properties

## I. INTRODUCTION

In Ce-based Kondo lattice systems a delicate interplay of localized and itinerant electronic degrees of freedom leads to a wealth of intriguing strongly correlated electron phenomena.<sup>1–6</sup> Kondo lattice compounds contain Ce ions arranged periodically in a crystal lattice. Thus, local  $f$ -moments of the  $\text{Ce}^{3+}$  ions can mutually couple via the conduction electrons by means of the Ruderman-Kittel-Kasayama-Yosida (RKKY) interaction.<sup>7</sup> Simultaneously, the  $f$ -moments are screened by spins of conduction  $s$ -electrons. This antiferromagnetic (AFM) Kondo coupling drives the demagnetization of the  $f$ -electron states and leads to the formation of the Abrikosov-Suhl resonance near the Fermi level.<sup>1,2</sup>

Both the RKKY interaction and Kondo effect depend on the coupling constant  $J_{s-f}$  of the local  $f$ -moments with the conduction electron states, with the characteristic temperatures  $T_{\text{RKKY}} \sim J_{s-f}^2$  and  $T_{\text{K}} \sim \exp(1/|J_{s-f}|)$ , respectively.<sup>8</sup> In the weak coupling limit, the magnetic interaction dominates over the Kondo spin-compensation and a magnetic ground state results.<sup>1–3</sup> For medium  $J_{s-f}$  values, a strong competition between Kondo effect and magnetic interactions gives rise to diverse intriguing physical phenomena, including magnetism with reduced moments,<sup>3</sup> non-Fermi liquid behaviour<sup>5</sup> or magnetically driven superconductivity.<sup>3,4</sup> In turn, in the strong coupling limit, the Kondo effect predominates and leads to a nonmagnetic heavy-fermion (HF) ground state.<sup>1</sup> Importantly, for large  $J_{s-f}$  values

the strong hybridization between the  $4f$  and other conduction band states together with a proximity of the  $4f$  level to the Fermi energy may also trigger instabilities of the charge configuration of the Ce ions, resulting in an intermediate valence behaviour.<sup>6</sup> Thus, physical properties of intermediate-valent systems are governed by both spin fluctuations due to Kondo effect and charge fluctuations between  $4f^0$  and  $4f^1$  configurations that are nearly degenerate in energy.

While vast majority of Ce-based intermetallic compounds contains either trivalent or intermediate-valent Ce ions, only for a limited number of systems a coexistence of both species has been reported. Examples of such materials include  $\text{Ce}_2\text{RuZn}_4$ <sup>9,10</sup>,  $\text{Ce}_3\text{Ni}_2\text{Ge}_7$ <sup>11</sup>,  $\text{Ce}_{23}\text{Ru}_7\text{X}_4$  ( $X = \text{Mg}, \text{Cd}$ )<sup>12,13</sup>,  $\text{CeRuSn}$ <sup>14–16</sup>,  $\text{Ce}_5\text{Sn}_3$ <sup>17</sup>,  $\text{Ce}_7\text{T}_3$  ( $T$ -transition metal)<sup>18</sup>,  $\text{Ce}_{4-x}\text{Ru}_4\text{Ge}_{12+x}$ <sup>19</sup>. These systems often exhibit remarkable electronic and magnetic properties related to a mixture of Ce ions with long and extraordinarily short distances to the neighbouring atoms due to a peculiar bonding situation. Bearing this distinctive structural feature in mind, we started systematic investigations aiming at finding novel intermetallic compounds with highly unconventional magnetic behaviour resulting from the presence of Ce ions in different valence states.

We focused our search on the system Ce-Rh-Sn as it is rich in ternary phases that show a full spectrum of strongly correlated electron phenomena related to various strength of hybridization between Ce  $4f$  and other valence band states.<sup>20–27</sup>  $\text{CeRhSn}_2$ ,  $\text{Ce}_5\text{Rh}_4\text{Sn}_{10}$ ,  $\text{CeRh}_2\text{Sn}_4$  and  $\text{Ce}_3\text{Rh}_4\text{Sn}_{13}$  are magneti-

cally ordered Kondo lattice systems.<sup>20–23</sup> In contrast, for  $\text{Ce}_{3+x}\text{Rh}_4\text{Sn}_{13-x}$  ( $0.2 \lesssim x \lesssim 0.6$ ) no sign of Kondo effect or long range magnetic order was found even down to 0.4 K.<sup>25</sup> In turn, in  $\text{CeRhSn}$  the Ce ions are in an intermediate valence state.<sup>26,27</sup>

Here, we report on  $\text{Ce}_2\text{Rh}_3\text{Sn}_5$  that crystallizes in the orthorhombic  $\text{Y}_2\text{Rh}_3\text{Sn}_5$  type of structure, where Y ions occupy two distinct crystallographic sites.<sup>28,29</sup> An early study revealed a moderate HF behaviour ( $\gamma \approx 150 \text{ mJ Ce-mol}^{-1}\text{K}^{-2}$ ) with a magnetic transition at  $T_N \approx 5 \text{ K}$  (from resistivity), 4 K (from magnetic susceptibility) or 2.5 K (from heat capacity).<sup>28</sup> Our single crystal X-ray diffraction (XRD) study unveils extraordinarily short Ce–Rh contacts indicative of valence close to 4+ for one Ce site. Interestingly, the local environment of Ce atoms from the second sublattice is very similar to that in  $\text{CeRh}_2\text{Sn}_4$ , a magnetic Kondo lattice system with trivalent Ce ions and  $T_N \approx 3.2 \text{ K}$ .<sup>23</sup> Motivated by these results, we performed a combined experimental and theoretical study on  $\text{Ce}_2\text{Rh}_3\text{Sn}_5$  based on thermodynamic measurements and spectroscopic data together with first principles electronic structure calculations aiming at exploring its complex structural and magnetic properties.

## II. METHODS

### A. Experimental

Polycrystalline samples of  $\text{Ce}_2\text{Rh}_3\text{Sn}_5$  with total weight of about 2 g were prepared from ingots of cerium (Ames, 99.9 wt.%), rhodium granules (ChemPur, 99.9 wt.%) and tin foil (ChemPur, 99.995 wt.%). Stoichiometric amounts of the elemental metals were arc-melted on a water cooled copper hearth in an ultra-high purity Ar atmosphere with a Zr getter (heated above the melting point). The sample was remelted several times to promote homogeneity and heat-treated at 800°C for 14 days in a sealed Ta tube enclosed in an evacuated quartz tube. Almost no mass loss (below 0.02%) occurred during the melting and annealing processes.

All manipulations related to preparation of the sample and its storage were performed in a argon-filled glove box (MBRAUN,  $p(\text{O}_2/\text{H}_2\text{O}) \leq 1 \text{ ppm}$ ) in order to prevent the oxidation.

The quality of the sample was examined by means of powder XRD measurements and metallographic investigations. Details of these studies are included in the Supplementary Information<sup>30</sup>. Powder XRD pattern indicates that the sample is nearly single phased. Microprobe measurements revealed the chemical composition that corresponds to  $\text{Ce}_{2.01(1)}\text{Rh}_{3.00(2)}\text{Sn}_{5.00(2)}$  and thus confirms the desired stoichiometry.

An irregularly shaped crystal was mechanically extracted from the annealed ingot. Single crystal XRD study was performed at room temperature using an Xcalibur E Single Crystal Diffractometer. Details concerning data collection and handling are summarized in Ta-

ble I. Structure refinements were carried out using the Jana2006 program.<sup>33</sup>

The Ce  $L_{\text{III}}$  XAS spectra were recorded in transmission arrangement at the EXAFS beamline C of HASY-LAB at DESY at the temperatures of 80 K and 293 K. The wavelength selection was realized using the four-crystal mode which yielded an experimental resolution of  $\sim 2 \text{ eV}$  (FWHM) at the Ce  $L_{\text{III}}$  threshold of 5723 eV. Powdered samples of  $\text{Ce}_2\text{Rh}_3\text{Sn}_5$  were mixed with small amounts of  $\text{B}_4\text{C}$  and mounted on  $1 \text{ cm}^2$  window sample holders using paraffin wax. Two series of measurements performed using different sample powders at ambient temperature and at low temperatures down to 6 K using a helium gas flow cryostat gave consistent results. Experimental data were recorded with  $\text{CePO}_4$  as the external reference compound with  $\text{Ce}^{3+}$  ions. The Ce  $L_{\text{III}}$  XAS spectra were evaluated using the Athena program package<sup>34</sup>.

XPS experiments were performed at room temperature using a PHI 5700 ESCA spectrometer with monochromatized  $\text{Al K}_\alpha$  radiation. The energy resolution was about 0.4 eV. The polycrystalline sample was broken under a high vacuum of  $6 \times 10^{-10}$  Torr immediately before measuring the spectra. Binding energies were referenced to the Fermi level ( $\epsilon_F = 0$ ). Calibration of the spectra was performed according to Ref. 35.

The magnetization studies were carried out in a SQUID magnetometer (MPMS XL-7, Quantum Design) at temperatures between 1.8 K and 400 K in magnetic fields up to 70 kOe. Electrical resistivity measurements were performed with a standard dc four-probe setup. Heat capacity was determined by a relaxation-type method using a commercial system (PPMS, Quantum Design).

### B. Computational

The electronic structure of  $\text{Ce}_2\text{Rh}_3\text{Sn}_5$  was studied using the Full Potential Local Orbital (FPLO) Minimum Basis code<sup>36</sup>. Scalar-relativistic calculations were performed within the local (spin) density approximation [L(S)DA] using the Perdew and Wang<sup>37</sup> parametrization of the exchange–correlation (XC) potential as well as within the generalized gradient approximation (GGA) as implemented by Perdew, Burke and Ernzerhof (PBE96)<sup>38</sup>. The strong Coulomb correlation within the Ce  $4f$  shell was also treated in a mean field approximation using the LSDA+U method<sup>39</sup> with the around mean field double counting scheme. The Coulomb repulsion  $U$  and exchange constant  $J$  for the  $4f$  states of both types of Ce atoms were assumed to be 3.5–8 eV and 0–1 eV, respectively. Within this range of parameters, no significant changes of the electronic structure apart from the exact position of the Ce  $4f$  levels were observed. The Brillouin zone sampling was based on 198  $\mathbf{k}$ -points in the irreducible wedge (2000 points in the full zone). A series of calculations with an increasing density

TABLE I. Crystallographic data for  $\text{Ce}_2\text{Rh}_3\text{Sn}_5$ .

Empirical formula	$\text{Ce}_2\text{Rh}_3\text{Sn}_5$
Structure type	$\text{Y}_2\text{Rh}_3\text{Sn}_5$
Space group	$Cmc2_1$ (No. 36)
Lattice parameters <sup>a</sup>	$a = 4.4992(1) \text{ \AA}$ $b = 26.4839(7) \text{ \AA}$ $c = 7.2160(2) \text{ \AA}$
Unit cell volume, <sup>a</sup> $V$	$859.83(4) \text{ \AA}^3$
Formula units/cell, $Z$	4
Crystal density, $\rho$	$9.151 \text{ g cm}^{-3}$
Temperature	$295(5) \text{ K}$
Diffraction system	Xcalibur E, four-circle Kappa Sapphire CCD Detector (Xcalibur)
Radiation, $\lambda$	$\text{Mo } K\alpha$ , $0.71073 \text{ \AA}$
Range in $h, k, l$	$\pm 9, \pm 52, \pm 14$
$R(eq\upsilon)/R(\sigma)$	0.078/0.018
$2\theta_{min}/2\theta_{max}$	4.17/45.49
Observation criteria	$F(hkl) > 3.00\sigma(F)$
Resolution $d$ ( $\text{\AA}$ )	0.45
Absorption correction	face-based, analytical <sup>31</sup>
Absorption coefficient	30.194
$N(hkl)$ measured	71975
$N(hkl)$ unique	3939
Extinction method	isotropic type 2 correction <sup>32</sup>
Extinction coefficient	4070(70)
Number of parameters	63
Goodness-of-fit (GOF)	1.94
R	2.25%
wR	3.28%

<sup>a</sup>powder data

of the  $\mathbf{k}$ -mesh was performed to ensure the convergence of the total energy with respect to the  $\mathbf{k}$ -grid.

Based on the band structure results we estimated the theoretical XPS valence band spectra. The partial  $l$ -resolved densities of states obtained using the LDA and the LSDA+U ( $U=6 \text{ eV}$ ,  $J=1 \text{ eV}$ ) methods were weighted by their respective photoionisation cross-sections<sup>40</sup>. The results were multiplied by the Fermi-Dirac function for 300 K and convoluted by Lorentzians with a full width at half maximum (FWHM) of 0.4 eV to account for the instrumental resolution, thermal broadening and the lifetime effect of the hole states.

### III. RESULTS AND DISCUSSION

#### A. Crystal structure

Refinement of the single crystal XRD data shows that  $\text{Ce}_2\text{Rh}_3\text{Sn}_5$  crystallizes with the non-centrosymmetric orthorhombic  $\text{Y}_2\text{Rh}_3\text{Sn}_5$  type of structure (space group  $Cmc2_1$ ), in agreement with earlier reports.<sup>28,29</sup> The crys-

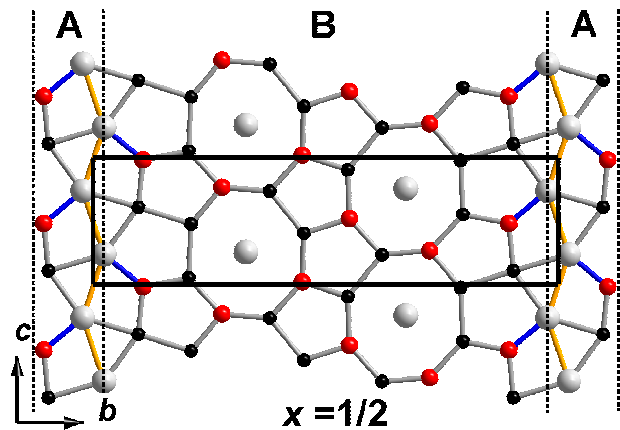


FIG. 1. (Color online) The planar layer in the structure of  $\text{Ce}_2\text{Rh}_3\text{Sn}_5$  occurring at  $x = 1/2$ . Fragment A: a chain of interconnected Ce atoms (yellow line) and edge sharing tetragons and triangles; fragment B: condensed empty pentagons and octagons of Rh (red) and Sn (black) centred by Ce (grey) atoms.

tallographic details of the refinement are given in Table I, atomic coordinates and anisotropic displacement parameters – in Table II and interatomic distances in Table III.

The  $\text{Y}_2\text{Rh}_3\text{Sn}_5$  type is a layered structure consisting of two analogical layers shifted by  $1/2$  of the translation in the  $bc$ -plane and alternating along  $x$ -direction. As indicated in Fig. 1, each layer consists of two main fragments: A (a chain of interconnected  $\text{Y}_2/\text{Ce}_2$  atoms and edge sharing tetragons and triangles) and B (condensed pentagons and octagons). The octagons are centred by heavy  $\text{Y}_1/\text{Ce}_1$  atoms, while pentagons remains empty. The B-fragments are very similar to layers formed by octagons and pentagons in the structure of the  $\text{NdRh}_2\text{Sn}_4$  type. The close structural relationship of  $\text{Y}_2\text{Rh}_3\text{Sn}_5$  and  $\text{NdRh}_2\text{Sn}_4$  types is widely discussed in the literature.<sup>23,29,43</sup>

The interatomic distances in the structure of  $\text{Ce}_2\text{Rh}_3\text{Sn}_5$  (Table III) mostly correlate well with the sum of atomic radii of the elements [ $r_{(\text{Ce})} = 1.825 \text{ \AA}$ ;  $r_{(\text{Rh})} = 1.34 \text{ \AA}$ ;  $r_{(\text{Sn})} = 1.41 \text{ \AA}$ ]<sup>44</sup>. The Sn-Sn contacts are slightly longer than  $2.81 \text{ \AA}$ , while the Rh-Sn distances are shortened by about 4-5%, which assumes the formation of covalently bonded Rh-Sn framework in the investigated structure. The shrinking of Ce-Sn contacts is of 1-2%, assuming also a weak interaction.

The most intriguing feature of the  $\text{Ce}_2\text{Rh}_3\text{Sn}_5$  structure is the shortened Ce2-Rh2 distance by nearly 11%. Such extraordinarily short Ce2-Rh contacts are indicative of a Ce2 valence close to  $+4$ .<sup>6,27,45,46</sup> In turn, for Ce1 ions all the Ce1-Sn and Ce1-Rh distances are nearly equal to the sum of corresponding atomic radii. This suggests that the electronic configuration for Ce1 ions is close to  $4f^1$ , i.e.  $\text{Ce}^{+3}$ . Thus, the analysis of the crystal structure indicates that  $\text{Ce}_2\text{Rh}_3\text{Sn}_5$  may be a mixed valence, intermediate valence or even a multivalent charge-

TABLE II. Atomic positional and displacement parameters for  $\text{Ce}_2\text{Rh}_3\text{Sn}_5$  (Note:  $B_{12}=B_{23}=0.$ ) All atoms are located at  $4a$  (0,y,z) Wyckoff positions. The experimental structural data are compared to those derived from the band structure calculations in the LDA approximation. The free parameters in atomic coordinates obtained from the computational study were rounded to three significant digits.

Atom	experiment							LDA	
	$y$	$z$	$B_{11}$	$B_{22}$	$B_{33}$	$B_{23}$	$B_{iso}$	$y$	$z$
Ce1	0.32754(1)	0.27397(5)	0.72(1)	0.77(1)	0.98(1)	-0.02(1)	0.82(1)	0.330	0.274
Ce2	0.02426(1)	0.25076(4)	0.93(1)	0.77(1)	0.81(1)	-0.08(1)	0.84(1)	0.026	0.239
Rh1	0.72296(2)	0.28274(6)	0.75(1)	0.74(1)	0.87(2)	-0.06(1)	0.79(1)	0.723	0.280
Rh2	0.10594(2)	0.00000(6)	1.06(2)	0.82(1)	0.94(2)	0.01(1)	0.94(1)	0.103	0.999
Rh3	0.44897(2)	0.03180(6)	0.78(1)	0.82(1)	0.80(2)	0.00(1)	0.80(1)	0.450	0.015
Sn1	0.21037(1)	0.49104(5)	0.80(1)	0.82(1)	0.73(1)	-0.07(1)	0.78(1)	0.210	0.491
Sn2	0.20563(1)	0.07177(6)	0.71(1)	0.82(1)	0.79(1)	0.09(1)	0.77(1)	0.205	0.065
Sn3	0.62182(1)	0.25218(6)	1.41(1)	0.69(1)	0.93(1)	-0.09(1)	1.01(1)	0.622	0.242
Sn4	0.45116(1)	0.41543(6)	0.86(1)	0.73(1)	0.77(1)	0.01(1)	0.79(1)	0.452	0.400
Sn5	0.09635(1)	0.62444(6)	0.77(1)	0.76(1)	0.99(1)	0.16(1)	0.84(1)	0.096	0.618

TABLE III. Selected interatomic distances in  $\text{Ce}_2\text{Rh}_3\text{Sn}_5$ .

Atoms	$d$ (Å)	Atoms	$d$ (Å)
Ce1 – 2Sn1	3.1979(4)	1Ce1	3.4733(5)
		2Sn5	3.2060(4)
		2Sn2	3.2310(4)
		1Sn4	3.4268(5)
		1Sn1	3.4733(5)
		1Sn2	3.5402(5)
		2Rh2	3.2885(4)
Ce2 – 2Sn4	3.1954(3)	Sn2 – 2Ce1	3.2310(4)
		1Ce1	3.5402(5)
		1Sn1	3.0255(5)
		2Sn1	3.2155(4)
		2Sn4	3.3656(4)
		1Rh2	2.6885(6)
		2Rh1	2.7537(4)
		1Rh1	2.8132(6)
		2Rh3	3.1091(4)
Rh1 – 1Sn3	2.6854(5)	Sn3 – 2Ce2	3.4243(4)
		1Sn4	3.1024(5)
		1Rh1	2.6854(5)
		1Rh3	2.7522(6)
		2Rh2	2.9226(4)
		Sn4 – 2Ce2	3.1954(3)
Rh2 – 1Ce2	2.8180(5)	2Ce2	3.3656(4)
		1Ce1	3.4268(5)
		1Sn3	3.1024(5)
		1Rh3	2.7665(6)
		1Rh3	2.7729(6)
		2Rh2	2.7774(3)
		2Sn3	2.9226(4)
Rh3 – 2Ce2	3.1091(4)	Sn5 – 2Ce1	3.2060(4)
		1Ce2	3.3012(5)
		1Ce2	3.3190(5)
		1Sn1	3.1670(5)
		1Sn4	2.7665(6)
		2Rh3	2.6350(3)
		1Rh2	2.7196(6)
Sn1 – 2Ce1	3.1979(4)		

ordered system. The last scenario assumes a static ordering of trivalent and intermediate-valent Ce ions in two distinct lattice sites and was proposed for systems such as  $\text{Ce}_2\text{RuZn}_4$ <sup>9,10</sup>,  $\text{Ce}_3\text{Ni}_2\text{Ge}_7$ <sup>11</sup>,  $\text{Ce}_{23}\text{Ru}_7\text{X}_4$  ( $X = \text{Mg}, \text{Cd}$ )<sup>12,13</sup>,  $\text{Ce}_5\text{Sn}_3$ <sup>17</sup>,  $\text{YbPtGe}_2$ .<sup>47</sup>

To inspect the valence states of Ce ions in  $\text{Ce}_2\text{Rh}_3\text{Sn}_5$  more closely, we performed spectroscopic measurements.

## B. Ce $L_{\text{III}}$ XAS

Fig. 2 presents the near-edge regime of Ce  $L_{\text{III}}$  XAS spectra for  $\text{Ce}_2\text{Rh}_3\text{Sn}_5$  that were recorded at several temperatures between 6 K and 300 K. Although the spectra are dominated by 'white line' at the energy of  $\sim 5726$  eV corresponding to  $4f^1$  configuration of  $\text{Ce}^{3+}$ , there is also an additional contribution at the energy of nearly +9 eV above the 'white line' maximum that indicates the presence of  $\text{Ce}^{4+}$  species with electron configuration  $4f^0$ . Increasing temperature from 6 K to 300 K leads to a gradual reduction of the high energy contribution due to  $4f^0$  configuration of  $\text{Ce}^{4+}$  and a simultaneous slight increase in intensity of the 'white line', as shown in Fig. 2b. Such a progressive shift of the spectral weight to lower energies implies an intermediate valence behaviour.

Deconvolution of the Ce  $L_{\text{III}}$  XAS spectra (example in Fig. 2a) indicates that the mean Ce valence in  $\text{Ce}_2\text{Rh}_3\text{Sn}_5$  decreases from +3.09(1) at 6 K to +3.04(1) at ambient temperature, with the most rapid changes taking place at temperatures of 100 K (see inset in Fig. 2(b)). Similar small valence changes were reported for many Ce- and Yb-based intermediate valence compounds.<sup>46,48-50</sup>

To shed more light on the character of Ce  $4f$  states in  $\text{Ce}_2\text{Rh}_3\text{Sn}_5$ , we performed X-ray photoelectron spectroscopy measurements.

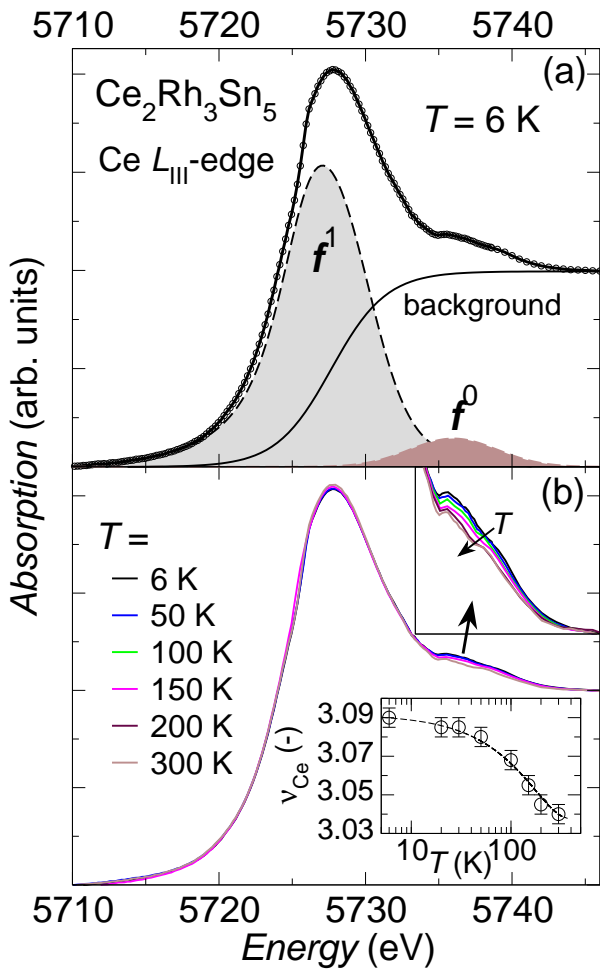


FIG. 2. (Color online) Near-edge regime of Ce  $L_{\text{III}}$  XAS spectra for  $\text{Ce}_2\text{Rh}_3\text{Sn}_5$ . Panel (a) shows deconvolution of the normalized spectrum recorded at  $T = 6$  K. The contributions due to  $f^1$  and  $f^0$  configurations are indicated by beige or grey fields underneath the dashed lines, while the solid black line represents the arctan function that accounts for transitions of  $2p_{3/2}$  electrons to the extended conduction states. Panel (b) depicts normalized Ce  $L_{\text{III}}$  XAS spectra measured at various temperatures between 6 K and 300 K. The changes in intensity of the  $f^0$  contribution are enlarged in the upper inset, with the arrow indicating the direction of increasing temperature. Lower inset of panel (b) displays calculated changes of Ce valence as a function of temperature. The dashed line was guided to the eye.

### C. Ce 3d XPS

Fig. 3 shows room temperature Ce 3d XPS spectrum for  $\text{Ce}_2\text{Rh}_3\text{Sn}_5$  together with the data for the structurally related compound  $\text{CeRh}_2\text{Sn}_4$ . Due to the spin-orbit (SO) coupling, Ce 3d states give rise to two sets of photoemission lines that correspond to the  $j = 3/2$  and  $j = 5/2$  components of final states. Each of these SO sets consists of two distinct contributions labelled as  $f^1$  and  $f^2$ . The  $f^1$  components originate from the screening of the core hole by conduction electrons. The  $f^2$  satellites arise

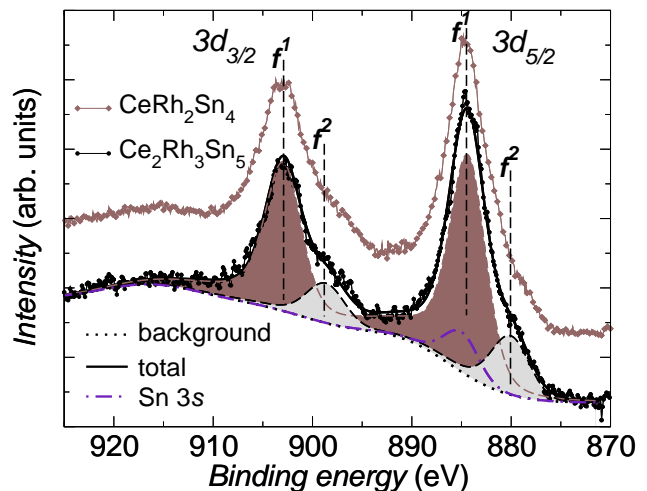


FIG. 3. (Color online) The Ce 3d XPS spectra for  $\text{Ce}_2\text{Rh}_3\text{Sn}_5$  and  $\text{CeRh}_2\text{Sn}_4$ . The spin-orbit components  $3d_{3/2}$  and  $3d_{5/2}$  as well as the  $f^1$  and  $f^2$  contributions are labelled. The deconvolution of the spectrum for  $\text{Ce}_2\text{Rh}_3\text{Sn}_5$  is shown.

when an electron is transferred from extended valence band states to the 4f states during photoemission process in order to screen the hole in the core shell. Since the probability of such processes depends on the coupling of the 4f levels to the other states near the Fermi level,<sup>45</sup> the presence of the pronounced  $f^2$  peaks indicates that there is a notable hybridization between the Ce 4f and conduction band states in  $\text{Ce}_2\text{Rh}_3\text{Sn}_5$ .

There are no additional peaks in the Ce 3d XPS spectrum of  $\text{Ce}_2\text{Rh}_3\text{Sn}_5$  in a distance of  $\sim 11$  eV from the main photoemission lines, that could be assigned to the  $4f^0$  final states. The absence of such extra peaks implies the occupancy of the Ce 4f shell  $n_f \lesssim 0.95$  at room temperature, in-line with the results of our XAS study (see Section III B).

Deconvolution of the Ce 3d XPS spectrum was performed on the basis of Doniach-Šunjić theory<sup>51</sup>. The intensity ratio  $I(3d_{5/2})/I(3d_{3/2}) = 3/2$  was fixed during the fitting, as required by the quantum-mechanical rules. The SO split  $\delta_{S-O} \approx 18.6$  eV was assumed. A Tougaard-type background<sup>52</sup> was subtracted from the XPS data. A small peak due to the Sn 3s states located at the binding energy of 885 eV was included in the fit, with the intensity determined by the stoichiometry of the compound  $\text{Ce}_2\text{Rh}_3\text{Sn}_5$ . Model calculations of Gunnarsson and Schönhammer (GS)<sup>45,53</sup> were used to calculate the value of the  $\Delta$  parameter describing the hybridization strength between the Ce 4f shell and conduction electron states from relative intensities of the  $f^2$  peaks. Such a procedure yielded  $\Delta \approx 100$  meV.

Since the measured XPS spectra contain signals originating from all Ce ions, the estimated  $\Delta$  value should be interpreted as the *average* hybridization parameter for Ce ions occupying two lattice sites in  $\text{Ce}_2\text{Rh}_3\text{Sn}_5$ . We note that the obtained  $\Delta$  value is comparable to those found in systems with Ce in an intermediate valence

state ( $\Delta \gtrsim 100$  meV)<sup>26,27,45</sup> and is notably stronger than in other compounds from the ternary Ce–Rh–Sn system with trivalent Ce ions ( $\Delta \lesssim 80$  meV)<sup>20,22–25</sup>. In particular, the  $\Delta$  value for  $\text{Ce}_2\text{Rh}_3\text{Sn}_5$  is larger than that for the structurally related compound  $\text{CeRh}_2\text{Sn}_4$  with  $\text{Ce}^{3+}$ , as evidenced directly by larger intensities of  $f^2$  satellites in the Ce  $3d$  XPS spectra (see Fig. 3).

Despite the strong hybridization  $\Delta$  and valence fluctuations revealed by our spectroscopic investigations, thermodynamic measurements indicate a magnetic ground state for  $\text{Ce}_2\text{Rh}_3\text{Sn}_5$ .

#### D. Magnetic measurements

Figures 4 and 5 present results of a *dc* magnetization study on polycrystals of  $\text{Ce}_2\text{Rh}_3\text{Sn}_5$ . The  $M(T)$  measured in weak magnetic fields increases rapidly at temperatures below  $\sim 2.9$  K, suggestive of an onset of magnetic order (see Fig. 4a). Closer inspection shows that the  $M(T)$  grows even faster at  $T \leq 2.4$  K. This points to a change in magnetic structure at 2.4 K, in agreement with our specific heat data that revealed two anomalies at  $T_{N1} \approx 2.9$  K and  $T_{N2} \approx 2.4$  K (see Section III E). The presence of two magnetic transitions in  $\text{Ce}_2\text{Rh}_3\text{Sn}_5$  provides an explanation for the discrepancy between ordering temperatures reported by Patil *et al.*<sup>28</sup> based on the specific heat and magnetization data.

Isothermal magnetization curves measured at temperatures below 3 K show distinct hysteresis between the data collected with increasing and decreasing field strengths. The illustrative  $M(H)$  data recorded at  $T = 1.8$  K are shown in Fig. 4b. Both the remanence magnetization  $M_r$  and the coercive field decrease gradually with increasing temperature and finally diminish at  $T_{N1} \approx 2.9$  K (see the lower inset of Fig. 4b). However, the magnetization in the ordered states is very small, about two orders of magnitude smaller than magnetization values expected for a ferromagnetic order that involves one magnetic ion per formula unit with  $S = 1/2$ . Thus, the magnetization measurements suggest an AFM ordering with only small canting in  $\text{Ce}_2\text{Rh}_3\text{Sn}_5$  at temperatures below 2.4 K, with the canting becoming even smaller between 2.4 K and 2.9 K.

At temperatures above  $\sim 8$  K, the magnetic susceptibility  $\chi = M/H$  plotted as a function of temperature resembles behaviour expected for a system with fluctuating magnetic moments (see inset of Fig. 4). However, attempts to describe the  $\chi(T)$  over a broad temperature range using a modified Curie–Weiss law do not give satisfactory results. Since our spectroscopic study revealed strong  $s$ – $f$  coupling and an intermediate valence behaviour (see Sections III B, III C), we used calculations of Rajan<sup>54</sup> based on the Coqblin–Schrieffer model to account for the presence of Ce ions with a Kondo singlet ground state. As there are two Ce sublattices in  $\text{Ce}_2\text{Rh}_3\text{Sn}_5$ , we attempted to fit the experimental mag-

netic susceptibility as:

$$\chi(T) = \frac{C}{T - \theta} + \chi_{\text{VF}}(T), \quad (1)$$

with the first term describing Curie–Weiss behaviour anticipated for  $\text{Ce}^{3+}$  and the term  $\chi_{\text{VF}}(T)$  calculated based on  $\chi_{\text{VF}}(T/T_0)/\chi(0)$  curve<sup>54</sup> for Ce impurity with  $j = 5/2$  in a metal with a nonmagnetic HF ground state. Here,  $T_0$  stands for strong-coupling scale that reflects the strength of Kondo interaction and  $\chi(0)$  denotes the value of magnetic susceptibility at zero temperature, where the Ce  $4f$  states of nonmagnetic Ce ions are delocalized into the conduction band and a heavy Fermi–liquid (FL) state forms. An excellent fit to the experimental  $\chi(T)$  data was achieved assuming that  $T_0 \approx 280$  K,  $\chi(0) \approx 0.0035$  emu/mol, the paramagnetic Weiss temperature  $\theta \approx -6$  K and the Curie constant  $C = 0.48$  emu K/mol-Ce (see Fig. 4).

The negative Weiss temperature of -6 K is comparable with the magnetic ordering temperatures and concurs with the dominance of weak AFM exchange interactions. The estimated  $C$  value corresponds to the fluctuating moment of  $1.96 \mu_B$  per Ce, which is somewhat smaller than the magnetic moment of  $2.54 \mu_B$  expected for free  $\text{Ce}^{3+}$  ions. We attribute this lowering of the effective moment to a crystal electric field (CEF) effect on magnetic Ce ions. Reduced values of the effective moment were reported also for an isostructural and isoelectronic compound  $\text{Ce}_2\text{Rh}_3\{\text{Pb},\text{Bi}\}_5$  in which  $\text{Ce}^{3+}$  ions experience strong CEF interactions.<sup>55</sup>

We note that the temperature of the maximum in  $\chi_{\text{VF}}(T)$  of  $\sim 80$  K agrees well with the value of the ratio  $C(\text{Ce}^{3+})/(3\chi(0)) \approx 76$  K, where  $C(\text{Ce}^{3+})$  is the Curie constant for  $\text{Ce}^{3+}$ . Such a scaling was observed for many intermediate valence systems with nearly trivalent Ce.<sup>6</sup> Thus, it provides a further indication for the reliability of the fit.

Finally, the performed analysis of  $\chi(T)$  indicates that the low temperature magnetic properties of  $\text{Ce}_2\text{Rh}_3\text{Sn}_5$  can be explained as a superposition of the enhanced Pauli paramagnetism due to delocalized  $4f$  electrons of half of the Ce ions and a magnetic order due to local moments of the remaining  $\text{Ce}^{3+}$  ions being a subject of strong CEF effect. To further test this scenario, we performed specific heat measurements.

#### E. Specific heat

Fig. 6 shows the low temperature specific heat data for  $\text{Ce}_2\text{Rh}_3\text{Sn}_5$ . A distinct anomaly in the  $C_p(T)$  curve at 2.4 K and a shoulder at 2.9 K are consistent with results of magnetic measurements (see Section III D) and indicate that  $\text{Ce}_2\text{Rh}_3\text{Sn}_5$  undergoes two magnetic transitions. However, the low temperature specific heat is dominated by a broad contribution underneath the magnetic peaks. To inspect its origin, we perform quantita-

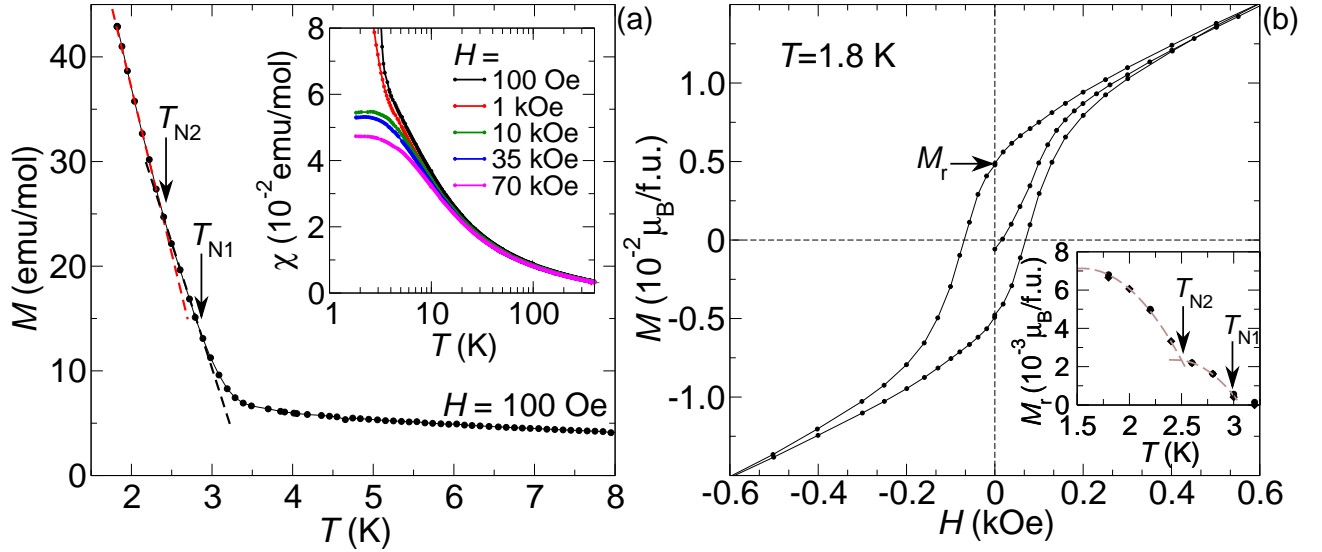


FIG. 4. (Color online) Results of *dc* magnetization measurements for  $\text{Ce}_2\text{Rh}_3\text{Sn}_5$ . Panel (a) shows the low temperature part of the  $M(T)$  measured in magnetic field of 100 Oe. Two distinct changes in slope of the  $M(T)$  curve suggestive of magnetic transitions are indicated. The inset displays the magnetic susceptibility measured in a number of magnetic fields between 100 Oe and 70 kOe and plotted as a function of temperature on a logarithmic scale. Panel (b) depicts the full magnetization loop at  $T = 1.8$  K. Inset shows values of the remanent magnetization at various temperatures. The dashed lines are guided to the eye.

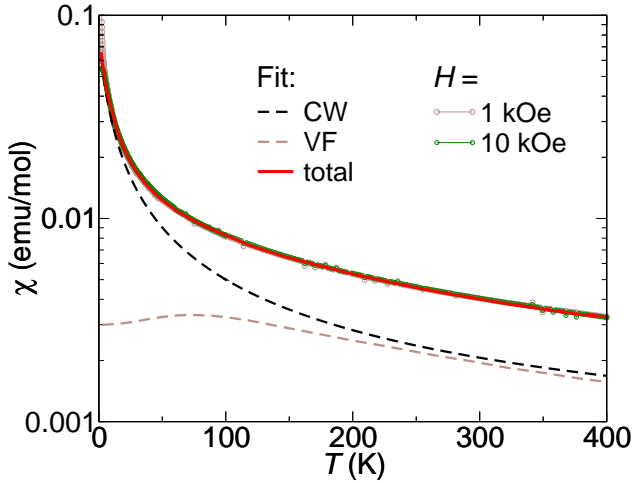


FIG. 5. (Color online) The *dc* magnetic susceptibility of  $\text{Ce}_2\text{Rh}_3\text{Sn}_5$  measured in magnetic fields of 1 kOe (brown circles) and 10 kOe (green circles), together with the fit using Equation 1 (thick solid red line). The contributions originating from  $\text{Ce}^{3+}$  (dashed black line labelled CW) and from intermediate-valent Ce ions (brown dashed line labelled VF) are shown separately.

tive analysis of different contributions to the low temperature specific heat.

First we evaluate the lattice and electronic specific heat. To this end, we plotted the  $C_p$  data in a  $C_p(T)/T$  representation (see Fig. 6b) and applied the Debye model. At temperatures between  $\sim 11$  K and  $\sim 20$  K, the experimental data follows the de-

pendence  $C_p/T = \gamma + \beta T^2 + \delta T^4$ , where the Sommerfeld coefficient  $\gamma \approx 110$  mJ/(mol K<sup>2</sup>) accounts for the electronic part of the specific heat and the consecutive two terms with  $\beta \approx 1.66 \times 10^{-3}$  mJ/(mol K<sup>4</sup>) and  $\delta \approx 4.04 \times 10^{-7}$  mJ/(mol K<sup>6</sup>) represent the first two terms in the Taylor expansion for the lattice specific heat. Although the fit was performed on the specific heat data at rather high temperatures, we note that the upper limit of the temperature range used for this analysis is only of 25% of the temperature at which  $\chi_{\text{VF}}(T)$  shows a maximum due to spin excitations from Kondo singlet ground state to  $j=5/2$  multiplet for nonmagnetic Ce ions (see Section III D). Further, the obtained  $\beta$  value corresponds to the Debye temperature of 227 K, which is close to Debye temperatures reported by Patil *et al.*<sup>28</sup> for isostructural and isoelectronic compounds with other rare earth elements.

To check whether the estimated  $\gamma$  value correlates with the enhancement of the zero-temperature magnetic susceptibility  $\chi(0) \approx 3.3 \times 10^{-3}$  emu/mol (see Section III D) and thus could be explained as due to itinerant *f* electrons in the FL state, we calculate the Sommerfeld-Wilson ratio  $R_{\text{SW}} = (\pi^2 k_B^2 / 3 \mu_{\text{eff}}^2) (\chi(0) / \gamma)$  using the free-ion value of the effective fluctuating moment  $\mu_{\text{eff}}$  of  $2.54 \mu_B$  per  $\text{Ce}^{3+}$  ion. The resulting  $R_{\text{SW}} \approx 1$  is typical for HF systems in which valence fluctuations between  $4f^0$  and  $4f^1$  configurations via strong hybridization between  $4f$  and conduction band states lead to the delocalization of the  $4f$  electrons, giving rise to an enhancement of the effective mass at low temperatures.<sup>56</sup>

The magnetic specific heat  $C_m(T)$  was calculated by subtracting from the total  $C_p(T)$  the estimated lattice



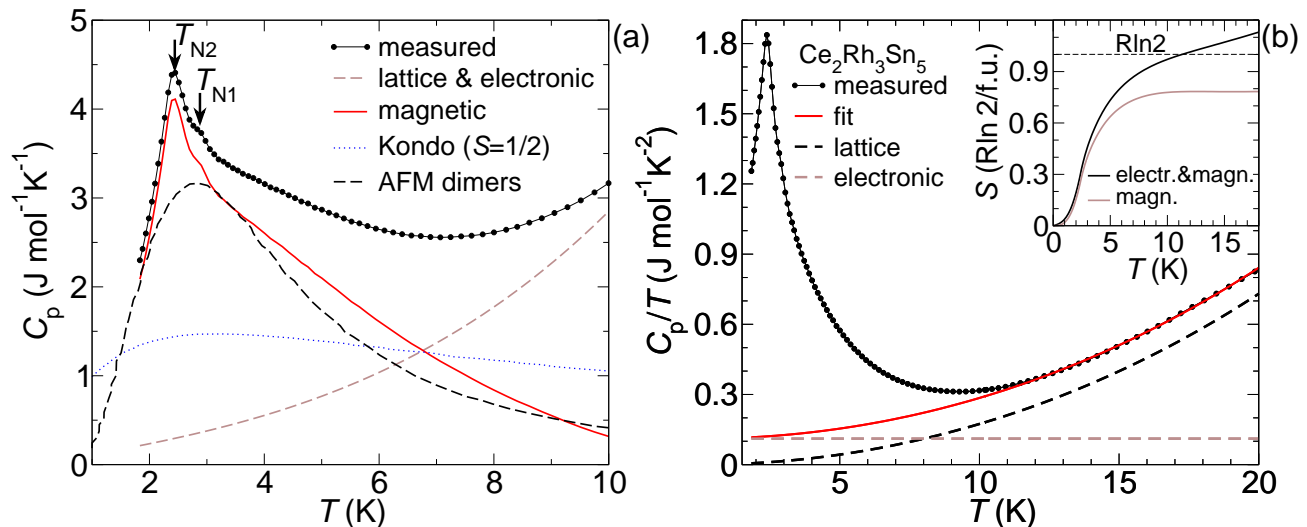


FIG. 6. (Color online) Low temperature specific heat of  $\text{Ce}_2\text{Rh}_3\text{Sn}_5$  shown as  $C_p(T)$  (panel a) and plotted in a conventional  $C_p/T(T)$  representation (panel b). The experimental data (black circles) are shown together with results of fits based on Debye model as described in the text. The magnetic contribution (red solid line) as well as fits based on Kondo model for  $S = 1/2$ <sup>58</sup> (blue dots) and simulation of the magnetic specific heat of AFM dimers (black dashed line) are also presented in panel a. The inset in panel b depicts the entropy per formula unit of  $\text{Ce}_2\text{Rh}_3\text{Sn}_5$  calculated from magnetic specific heat (solid brown line) and based on the sum of the electronic and magnetic specific heat (black solid line). The dashed horizontal line indicates the value of  $R\ln 2$  expected for one Ce ion a magnetic doublet ground state.

and electronic contributions (see Fig. 6a). The  $C_m(T)/T$  was extrapolated to  $T = 0$  and then integrated with respect to temperature to give an estimate for the low temperature magnetic entropy,  $S_m(T)$ . As shown in the inset of Fig. 6b, the  $S_m(T)$  saturates at the value of  $0.8 R\ln 2$  per formula unit. Even with the electronic specific heat term  $\gamma T$  included in the estimate, the magnetic entropy is only of  $R\ln 2$  per formula unit containing two Ce ions. This result implies that only half of Ce ions in  $\text{Ce}_2\text{Rh}_3\text{Sn}_5$  is in a CEF doublet ground state and contributes to the low temperature magnetic ordering.

The magnetic entropy saturates well above the magnetic transitions only, at  $T \approx 10$  K (see inset of Fig. 6b). Importantly, the value of the  $S_m$  recovered at  $T_{N2}=2.9$  K is only of  $0.40 R\ln 2$  per formula unit. Such a strong reduction of the magnetic entropy can be attributed to the Kondo effect on magnetic Ce ions and/or short range magnetic correlations that develop above magnetic ordering temperature. Assuming that the effect results solely from partial quenching of Ce  $4f$ -derived magnetic moments of  $\text{Ce}^{3+}$  ions by Kondo effect, the single-ion Kondo temperature for magnetic Ce ions estimated based on model calculations of Yashima *et al.*<sup>57</sup> for  $S = 1/2$  Kondo impurity should be of 7 K. However, attempts to describe the broad contribution to the magnetic specific heat based on the Kondo model<sup>58</sup> do not give satisfactory results (see Fig. 6a). Instead, the shape of the  $C_m(T)$  resembles magnetic anomalies observed for low dimensional systems.<sup>59,60</sup> As an example, Fig. 6a presents magnetic specific heat simulated for a system of AFM dimers with  $S = 1/2$  assuming that exchange coupling inside the dimers  $J/k_B \approx 5.7$  K and 75% of the

magnetic Ce ions are involved in the short range order. Close similarity between the calculated curve and the magnetic specific heat hints at a dominance of an AFM coupling between local moments of nearest neighbouring  $\text{Ce}^{3+}$  ions. On the other hand, a layered crystal structure of  $\text{Ce}_2\text{Rh}_3\text{Sn}_5$  composed of B blocks with trivalent Ce1 ions separated by A fragments containing nonmagnetic Ce2 ions (see Section III A) may facilitate quasi-two-dimensional magnetic correlations. Further studies including neutron diffraction and inelastic scattering measurements are needed to inspect in detail the low temperature magnetic order and magnetic excitations in  $\text{Ce}_2\text{Rh}_3\text{Sn}_5$ .

## F. Electrical resistivity

Fig. 7 shows the temperature dependence of the electrical resistivity measured on three polycrystalline blocks of  $\text{Ce}_2\text{Rh}_3\text{Sn}_5$ . The overall shape of the  $\rho(T)$  curves in conjunction with the values of the resistivity of  $\sim 200\text{--}300 \mu\Omega\text{cm}$  at lowest temperatures indicate a metallic behaviour of  $\text{Ce}_2\text{Rh}_3\text{Sn}_5$ , as expected based on the thermodynamic and spectroscopic data, and in agreement with previous report.<sup>28</sup>

For all the investigated specimens, the electrical resistivity shows broad maxima at  $T \sim 100$  K. At similar temperatures the XAS study revealed the fastest changes in Ce valence (see Section III B) and the  $\chi_{\text{VF}}(T)$  shows maximum due to excitations from Kondo singlet ground state to  $j=5/2$  multiplet (see Section III D). Therefore, we explain the strong scattering in this temperature range as



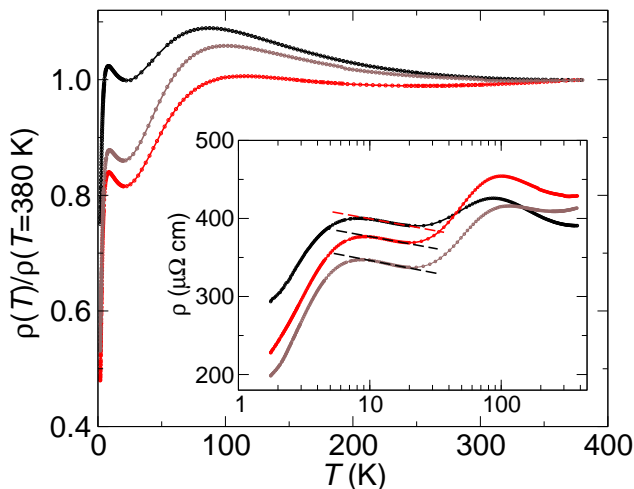


FIG. 7. (Color online) The electrical resistivity of  $\text{Ce}_2\text{Rh}_3\text{Sn}_5$  measured on three different polycrystalline blocks normalized to the value of the resistivity at 380 K. The inset shows the  $\rho(T)$  data plotted as a function of temperature on a logarithmic scale.

due to both charge and spin fluctuations associated with intermediate-valent Ce ions. Similar pronounced contributions to  $\rho(T)$  were observed for many Ce-based intermediate valence systems.<sup>6,46</sup>

At lower temperatures, the  $\rho(T)$  increases with decreasing temperature in a logarithmic fashion, as indicated in the inset of Fig. 7. Such logarithmic upturns signify the dominance of the  $-\ln T$  term resulting from incoherent Kondo scattering of conduction electrons on magnetic Ce ions.

Finally, the  $\rho(T)$  curves pass through maxima at temperatures of 8 K and fall rapidly with decreasing temperature. Such a temperature dependence of the resistivity is a typical manifestation of an onset of coherence between Kondo scattering centres arranged periodically in a crystal lattice.<sup>61</sup> The development of coherence governs the  $\rho(T)$  at temperatures close to the magnetic transitions, which may explain the lack of evidence for the magnetic transitions in the electrical resistivity curves.

### G. Fixed spin moment calculations

To get insight into magnetic properties of  $\text{Ce}_2\text{Rh}_3\text{Sn}_5$  from first principles, we performed a series of electronic band structure calculations within the LSDA approximation using the fixed spin moment (FSM) method. The total energies computed for different values of the FSM assuming the experimental crystal structure are shown in Fig. 8. There is a flat region in the total energy-versus-FSM curve ranging from 0 to about  $0.4 \mu_B$  per formula unit suggesting that  $\text{Ce}_2\text{Rh}_3\text{Sn}_5$  may be close to a magnetic instability.

Since calculated magnetic properties are often sensitive to atomic coordinates, we performed their computational

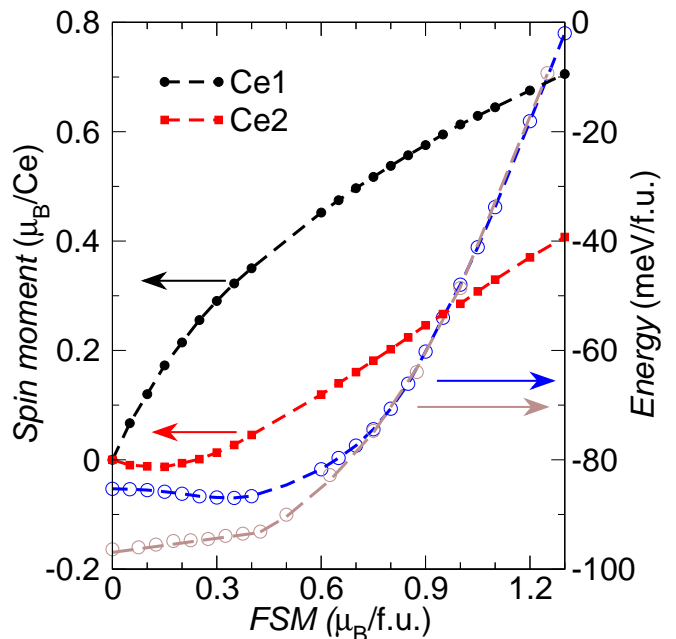


FIG. 8. (Color online) The total energy-versus-FSM curves derived from FSM calculations performed for  $\text{Ce}_2\text{Rh}_3\text{Sn}_5$  within the LSDA approximation assuming either the experimental crystal structure (empty beige circles) or the LDA crystal lattice (empty blue circles). The FSM values represent the total magnetic moments per formula unit. The total energy scale was shifted to allow for direct comparison of the curves obtained for the experimental and LDA crystal structures. The calculated values of Ce1 and Ce2 spin moments for the LDA crystal structure are shown as filled black circles and red squares, respectively. The dashed lines are guided to the eye.

relaxation based on atomic forces<sup>62</sup> to find theoretical equilibrium atomic positions for the LDA approximation. The resulting internal coordinates for which total force on each atom is smaller than 5 mRy/a.u. are listed in Table II. For this relaxed crystal structure, the LSDA calculations with initial spin-polarization converged to a magnetic state, that has now slightly lower total energy than the nonmagnetic solution ( $\Delta E \approx 1.7$  meV/f.u.). Indeed, for the LDA crystal structure there is a shallow magnetic minimum in the energy-versus-FSM curve at the FSM value of  $0.4 \mu_B$ /f.u., as shown in Fig. 8. Remarkably, for this magnetic state only Ce1 atoms exhibit significant spin moments, whereas Ce2 atoms as well as all Rh and Sn atoms in  $\text{Ce}_2\text{Rh}_3\text{Sn}_5$  stay almost unpolarized (spin moments below  $0.05 \mu_B$  per atom). Thus, our calculations indicate that only Ce1 sublattice contributes to the low temperature magnetic ordering in  $\text{Ce}_2\text{Rh}_3\text{Sn}_5$ .

### H. Valence band

Fig. 9 shows the total and partial atomic resolved DOSs for  $\text{Ce}_2\text{Rh}_3\text{Sn}_5$  calculated within the LDA approx-

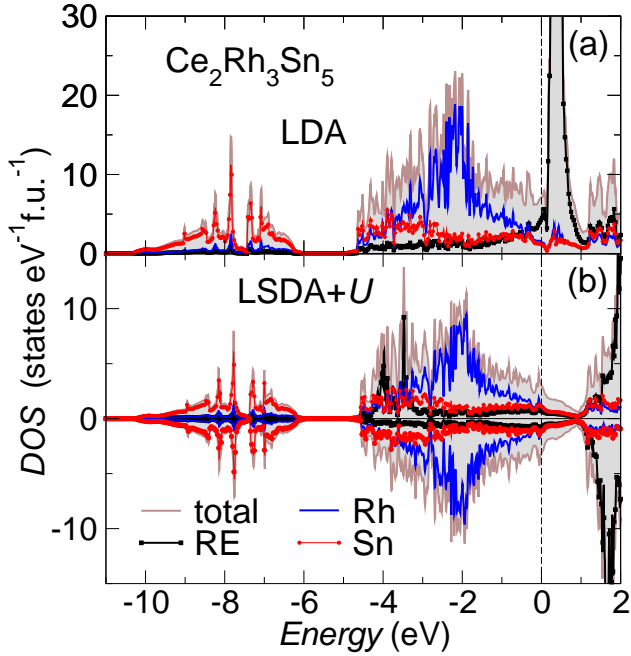


FIG. 9. (Color online) The total and atomic resolved DOSs for  $\text{Ce}_2\text{Rh}_3\text{Sn}_5$  calculated within the LDA approximation (panel (a)) and using the LSDA+ $U$  ( $U_{\text{eff}} = 6$  eV)<sup>63</sup> approach for the Ce 4 $f$  shell (panel (b)).

imation and using the LSDA+ $U$  approach to account for the strong Coulomb interaction within Ce 4 $f$  shell. The valence band of  $\text{Ce}_2\text{Rh}_3\text{Sn}_5$  consists of two parts separated by the gap of 1.5 eV. The structure at binding energies ranging from 5 to 8 eV originates primarily from 5 $s$  states of Sn atoms. The main part of the valence DOS is dominated by hybridized Rh 4 $d$  and Sn 5 $p$  states.

Within the LDA approximation, the Ce 4 $f$  states of both Ce1 and Ce2 form narrow peaks near the Fermi level. Inclusion of the Hubbard-like interaction terms to the XC potential results in a shift of the occupied Ce 4 $f$  bands toward higher binding energies and of the unoccupied 4 $f$  states above the Fermi level, as expected for a trivalent cerium. We note that none of our calculations (LDA or LSDA+ $U$ ) gives a proper description of the electronic structure of  $\text{Ce}_2\text{Rh}_3\text{Sn}_5$  in a region close to the Fermi level, where dynamic many-body effects play an essential role for the physical properties of Kondo lattice systems. To shed light on the effective mass enhancement in  $\text{Ce}_2\text{Rh}_3\text{Sn}_5$ , we estimate bare values of the Sommerfeld coefficient  $\gamma_b = (\pi^2/3)k_B\text{DOS}(E_F)$  using the  $\text{DOS}(E_F)$  derived from our calculations of 6–7 states per eV formula unit (Fig. 9). Comparison of the  $\gamma_b$  values of 15–17 mJ/(mol K<sup>2</sup>) with the experimental Sommerfeld coefficient in the paramagnetic region of 110 mJ/(mol K<sup>2</sup>) (see Section III E) shows that there is a notable mass enhancement in  $\text{Ce}_2\text{Rh}_3\text{Sn}_5$  which we attribute primarily to the formation of the Abrikosov–Suhl resonance near the Fermi energy due to Kondo effect. The Abrikosov–Suhl resonance can not be described in

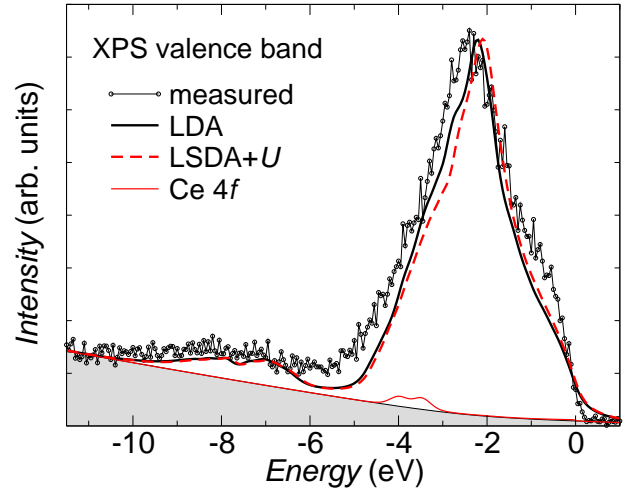


FIG. 10. (Color online) XPS valence band spectrum of  $\text{Ce}_2\text{Rh}_3\text{Sn}_5$  (thin black solid line with dots) in comparison with theoretical spectra calculated based on partial DOSs obtained within the LDA approximation (thick black line) and using the LSDA+ $U$  ( $U_{\text{eff}} = 6$  eV)<sup>63</sup> approach for the Ce 4 $f$  shell (thick dashed red line). The thin red (grey) solid line shows the sum of partial Ce1 4 $f$  and Ce2 4 $f$  contributions. The grey field represents background estimated using Tougaard algorithm<sup>52</sup>.

the applied static mean-field approximations which, by definition, neglect all dynamic correlation effects. Therefore, further theoretical study based on dynamical mean-field theory (DMFT) is needed to inspect the quasiparticle DOS near the Fermi level in  $\text{Ce}_2\text{Rh}_3\text{Sn}_5$ .

In order to gain experimental insight into the valence band of  $\text{Ce}_2\text{Rh}_3\text{Sn}_5$ , we performed photoemission measurements. Fig. 10 shows the XPS valence band spectrum for  $\text{Ce}_2\text{Rh}_3\text{Sn}_5$ . To facilitate its comparison with the band structure results, the theoretical XPS spectra were estimated based on the calculated partial DOSs as described in Section II B. The commonly used Tougaard-type<sup>52</sup> background (grey field in Fig. 10) was added to the calculated data to account for the presence of secondary electrons during photoemission processes. The exemplary results obtained based on DOSs calculated within the LDA approximation and using the LSDA+ $U$  ( $U_{\text{eff}} = 6$  eV) approach are presented in Fig. 10.

The calculated curves reflect all the essential features present in the measured XPS valence band spectrum, including the energy gap between the Sn 4 $s$ -like shallow core states and the remainder of the valence band. Thus, the experiment confirms the reliability of our computational results.

The Ce 4 $f$  contributions to the XPS valence band spectrum of  $\text{Ce}_2\text{Rh}_3\text{Sn}_5$  (Fig. 10) are very small as compared to the contributions from the other valence band states. Therefore, the XPS valence band spectrum can not give direct information about the localization of the Ce 4 $f$  states in the conduction band. We note, however, that the LDA approximation gives a somewhat better

match regarding energy positions of the main features in the XPS valence band spectrum than the LSDA+U approach. Further, the performed calculations indicate that the changes in the Ce2  $4f$  bands induced by application of the LSDA+ $U$  approach lead to a narrowing of the main part of the valence band and result in a shift of  $4d$  states of Rh2 and Rh3 towards lower binding energies, whereas the strength of correlation effects within the  $4f$  shell of Ce1 ions has almost no impact on the other valence band states (not shown). Thus, this study gives an indirect evidence for the important role of hybridization between Ce2  $4f$  and conduction band states near the Fermi level in  $\text{Ce}_2\text{Rh}_3\text{Sn}_5$ .

#### IV. CONCLUSIONS

The crystal structure of  $\text{Ce}_2\text{Rh}_3\text{Sn}_5$  was refined from single crystal XRD data. Analysis of interatomic distances and coordination of Ce atoms occupying two distinct crystallographic sites suggests that Ce1 species adopt the  $4f^1$  configuration ( $\text{Ce}^{3+}$ ), whereas the electronic configuration for Ce2 ions should be close to  $4f^0$  ( $\text{Ce}^{4+}$ ).

Thermodynamic measurements revealed a magnetic ground state. Both specific heat and magnetization data show two magnetic transitions at  $T_{N1} \approx 2.9$  K and  $T_{N2} \approx 2.4$  K. However, the low temperature magnetic entropy of  $\ln 2$  per formula unit implies that only half of Ce ions in  $\text{Ce}_2\text{Rh}_3\text{Sn}_5$  is in a CEF doublet ground state. Electronic structure calculations indicate that only Ce1 ions show local magnetic moments and contribute to the magnetic ordering, whereas Ce2 sublattice remains nonmagnetic. This result is further corroborated by the temperature dependence of the magnetic susceptibility which was successfully described assuming that only one Ce sublattice shows local moment paramagnetism anticipated for  $\text{Ce}^{3+}$ , whereas for the remaining Ce ions an enhanced Pauli paramagnetism ( $\chi(0) \approx 0.0035$  emu/mol) arises due to itinerant  $4f$  electrons.

The computational results in conjunction with the XPS spectra point to the importance of the hybridization between Ce2  $4f$  and other conduction band states in  $\text{Ce}_2\text{Rh}_3\text{Sn}_5$ , which is essential for the delocalization of the  $f$  states. The Sommerfeld coefficient  $\gamma \approx 110$  mJ/(mol K<sup>2</sup>) about seven times larger than the bare  $\gamma$  value obtained from the calculated DOS( $E_F$ ) indicates a moderate renormalization of quasiparticle masses, which we attribute to the formation of Abrikosov–Suhl

resonance due to Kondo effect. The Sommerfeld–Wilson ratio  $R_{\text{SW}} \approx 1$  provides further indication that the enhancement of both  $\chi(0)$  and  $\gamma$  is primarily associated with the itinerant  $f$  electrons in the FL state.

Deconvolution of Ce  $L_{\text{III}}$  XAS spectra shows that the mean Ce valence in  $\text{Ce}_2\text{Rh}_3\text{Sn}_5$  decreases from +3.09 at 6 K to +3.04 at ambient temperature. These values, however, should be interpreted as the *average* valence for Ce ions from both lattice sites in  $\text{Ce}_2\text{Rh}_3\text{Sn}_5$  as the measured spectra contain signal originating from all Ce ions. Therefore, assuming that Ce1 is trivalent in the entire temperature range, the valence of Ce2 species should vary between +3.18 at 6 K and +3.08 at  $\sim 300$  K. Remarkably, similar values of Ce valence were reported for an intermediate valence compound  $\text{CeRhSi}_2$ ,<sup>46</sup> for which the magnetic susceptibility closely resembles the  $\chi_{\text{VF}}(T)$  part of the  $\chi(T)$  for  $\text{Ce}_2\text{Rh}_3\text{Sn}_5$ . Furthermore, the temperature range with the fastest changes in Ce valence in  $\text{Ce}_2\text{Rh}_3\text{Sn}_5$  coincides well with the maximum in the  $\chi_{\text{VF}}(T)$ , suggesting similar energy scales for charge and spin excitations associated with intermediate–valent Ce ions. This conclusion agrees with the observation of Lawrence *et al.*,<sup>6</sup> that a single energy scale is sufficient for describing intermediate valence systems with Ce valence close to 3+.

Finally, our combined experimental and theoretical study indicates that  $\text{Ce}_2\text{Rh}_3\text{Sn}_5$  is a multivalent charge ordered Kondo lattice system in which magnetic behaviour due to trivalent Ce1 ions ( $4f^1$ ) coexists with valence fluctuations associated with Ce2 ions for which the ground state electronic configuration is close to  $4f^0$ . Further study is needed to elucidate in detail the electronic band structure of  $\text{Ce}_2\text{Rh}_3\text{Sn}_5$  near the Fermi level where dynamical many–body effects determine the shape of quasiparticle DOS and to shed more light on the magnetic ground state.

#### V. ACKNOWLEDGMENTS

The authors thank Dr Christoph Geibel from Max-Planck Institute for Chemical Physics of Solids for fruitful discussions. The authors are grateful to Dr Jerzy Kubacki from University of Silesia for his kind help with XPS measurements and to Dr E. Welter and Dr D. Zajac from HASYLAB for their helpful assistance during XAS measurements on beamline C of Hasylab, Desy. M. G. would like to acknowledge financial support from the Max–Planck Society and the DAAD foundation through research fellowships.

<sup>1</sup> G. Stewart, *Rev. Mod. Phys.* **73**, 797 (2001); A. Georges, G. Kotliar, W. Krauth, and M. J. Rozenberg, *Rev. Mod. Phys.* **68**, 13 (1996), and references therein.

<sup>2</sup> A.C. Hewson in: *The Kondo Problem to Heavy Fermions*, Cambridge University Press (1997).

<sup>3</sup> H.B. Radousky (Eds.) *Magnetism in Heavy Fermion Systems*, World Scientific Publishing Co. Ptd. Ltd., Singapore, 2000 (ISBN 981-02-4348-0).

<sup>4</sup> P. Monthoux, D. Pines, and G.G. Lonzarich, *Nature* **450**, 1177 (2007).

- <sup>5</sup> G.R. Stewart, *Rev. Mod. Phys.* **78**, 743 (2006).
- <sup>6</sup> J.M. Lawrence, P.S. Riseboroughs, and R.D. Parks, *Reports on Progress in Physics* **44**, 1 (1981) and references therein.
- <sup>7</sup> M.A. Ruderman and C. Kittel *Phys. Rev.* **96**, 99 (1954).
- <sup>8</sup> S. Doniach in: R.D. Parks (Eds.) *Valence Instability and Related Narrow Band Phenomena*, Plenum New York (1977) and references therein.
- <sup>9</sup> T. Mishra, W. Hermes, U. Ch. Rodewald, R.-D. Hoffmann, R. Pöttgen, *Z. Anorg. Allg. Chem.* **634**, 470 (2008).
- <sup>10</sup> V. Eyert, E.-W. Scheidt, W. Scherer, W. Hermes, R. Pöttgen, *Phys. Rev. B* **78**, 214420 (2008).
- <sup>11</sup> L. Durivault, F. Bourée, B. Chevalier, G. André, J. Etourneau, and O. Isnard, *J. Magn. Magn. Mat.* **232**, 139 (2001).
- <sup>12</sup> F. Tappe, W. Hermes, M. Eul, R. Pöttgen, *Intermetallics* **17**, 1035 (2009).
- <sup>13</sup> S. Linsinger, M. Eul, W. Hermes, R.-D. Hoffmann, and R. Pöttgen, *Z. Naturforsch.* **64b**, 1345 (2009).
- <sup>14</sup> S.F. Matar, J.F. Riecken, B. Chevalier, R. Pöttgen, A. F. Al Alam, V. Eyert, *Phys. Rev. B* **76**, 174434 (2007).
- <sup>15</sup> J.A. Mydosh, A.M. Strydom, M. Baenitz, B. Chevalier, W. Hermes, R. Pöttgen, *Phys. Rev. B* **83**, 054411 (2011).
- <sup>16</sup> R. Feyerherm, E. Dudzik, K. Prokeš, J.A. Mydosh, Y.-K. Huang, R. and Pöttgen, *Phys. Rev. B* **90**, 041104 (2014).
- <sup>17</sup> J.M. Lawrence, M.F. Hundley, J.D. Thompson, G.H. Kwei, and Z. Fisk, *Phys. Rev. B* **43**, 11057 (1991).
- <sup>18</sup> O. Trovarelli, J.G. Sereni, G. Schmerber and J.P. Kappler, *Physica B* **206/207**, 243 (1995).
- <sup>19</sup> K. Ghosh, S. Ramakrishnan, S.K. Dhar, S.K. Malik, G. Chandra, V.K. Pecharsky, K.A. Gschneidner, Jr., Z. Hu, and W.B. Yelon, *Phys. Rev. B* **52**, 7267 (1995).
- <sup>20</sup> M.B. Gamża, A. Ślebarski, and H. Rosner, *J. Phys.: Condens. Matter* **20**, 025201 (2008).
- <sup>21</sup> D. Niepmann, R. Pöttgen, B. Künnen, G. Kotzyba, C. Rosenhahn, and B.D. Mosel, *Chem. Mater.* **11**, 1597 (1999).
- <sup>22</sup> M.B. Gamża, A. Ślebarski, and H. Rosner, *Eur. Phys. J. B* **63**, 1 (2008).
- <sup>23</sup> M.B. Gamża, W. Schnelle, R. Gumeniuk, Yu. Prots, A. Ślebarski, H. Rosner, Yu. Grin, *J. Phys.: Condens. Matter* **21**, 325601 (2009).
- <sup>24</sup> M.B. Gamża, W. Schnelle, A. Ślebarski, U. Burkhardt, R. Gumeniuk, and H. Rosner, *J. Phys.: Condens. Matter* **20**, 395208 (2008).
- <sup>25</sup> M.B. Gamża *et al.*, to be published.
- <sup>26</sup> A. Ślebarski, N.A. Frederick, and M.B. Maple, *Philos. Mag. B* **82**, 1275 (2002); A. Ślebarski, J. Spalek, M.B. Gamża, and A. Hackemer, *Phys. Rev. B* **73**, 205115 (2006); J. Spalek, A. Ślebarski, J. Goraus, L. Spalek, K. Tomala, A. Zarzycki, and A. Hackemer, *Phys. Rev. B* **72**, 155112 (2005).
- <sup>27</sup> M.B. Gamża, A. Ślebarski, and H. Rosner *Eur. Phys. J. B* **67**, 483 (2009).
- <sup>28</sup> N.G. Patil and S. Ramakrishnan, *Phys. Rev. B* **59**, 12054 (1999).
- <sup>29</sup> M. Méot-Mayer, G. Venturini, B. Malaman, J. Steinmetz, and B. Roques, *Mat. Res. Bull.* **19**, 1181 (1984).
- <sup>30</sup> M.B. Gamża *et al.*, Supplementary Information.
- <sup>31</sup> R.C. Clark, and J.S. Reid, *Acta Cryst.* **A51**, 887 (1995).
- <sup>32</sup> P.J. Becker and P. Coppens, *Acta Cryst.* **A30**, 129 (1974).
- <sup>33</sup> V. Petricek, M. Dusek and L. Palatinus, *Z. Kristallogr.* **229(5)**, 345 (2014).
- <sup>34</sup> B. Ravel and M. Newville, *J. Syn. Rad.* **12**, 537 (2005).
- <sup>35</sup> Y. Baer, G. Bush and P. Cohn, *Rev. Sci. Instrum.* **46**, 466 (1975).
- <sup>36</sup> K. Koepf and H. Eschrig, *Phys. Rev. B* **59**, 1743 (1999).
- <sup>37</sup> J.P. Perdew and Y. Wang, *Phys. Rev. B* **45**, 13244 (1992).
- <sup>38</sup> J.P. Perdew, K. Burke and M. Ernzerhof, *Phys. Rev. Lett.* **77**, 3865 (1996).
- <sup>39</sup> H. Eschrig, K. Koepf, and I. Chaplygin, *J. Solid State Chem.* **176**, 482 (2003).
- <sup>40</sup> J.J. Yeh and J. Lindau, *At. Data Nucl. Data Tables* **32**, 1 (1985).
- <sup>41</sup> D. Singh, *Plane waves, pseudopotentials and the LAPW method* (Kluwer Academic, 1994).
- <sup>42</sup> P. Blaha, K. Schwarz, G. Madsen, D. Kvasnicka and J. Luitz, *Program for calculating crystal properties WIEN2k*, Vienna University of Technology, 2001 (ISBN 3-9501031-1-2).
- <sup>43</sup> R.V. Skolozdra, *Handbook on the Physics and Chemistry of Rare Earth* **24**, (167), 400, edited by Gschneider K A, Jr. and Eyring L, North-Holland, Amsterdam (1997).
- <sup>44</sup> J. Emsley, *The Elements*, Oxford Univ. Press (1998).
- <sup>45</sup> J.C. Fuggle, F.U. Hillebrecht, Z. Zolnieriek, R. Lässer, Ch. Freiburg, O. Gunnarsson and K. Schönhammer, *Phys. Rev. B* **27**, 7330 (1983); A.J. Signorelli and R.G. Hayes, *Phys. Rev. B* **8**, 81 (1973).
- <sup>46</sup> D. Kaczorowski, A.P. Pikul, U. Burkhardt, M. Schmidt, A. Ślebarski, A. Szajek, M. Werwiski, and Yu. Grin, *J. Phys.: Condens. Matter* **22**, 215601 (2010).
- <sup>47</sup> R. Gumeniuk, R. Sarkar, C. Geibel, W. Schnelle, C. Paulmann, M. Baenitz, A.A. Tsirlin, V. Guritanu, J. Sichelschmidt, Yu. Grin, and A. Leithe-Jasper, *Phys. Rev. B* **86**, 235138 (2012); R. Sarkar, R. Gumeniuk, A. Leithe-Jasper, W. Schnelle, Yu. Grin, C. Geibel, and M. Baenitz, *Phys. Rev. B* **88**, 201101 (2013).
- <sup>48</sup> H. Yamaoka, I. Jarrige, N. Tsujii, N. Hiraoka, H. Ishii, and K.-D. Tsuei, *Phys. Rev. B* **80**, 035120 (2009).
- <sup>49</sup> W.B. Jiang, L. Yang, C.Y. Guo, Z. Hu, J.M. Lee, M. Smidman, Y.F. Wang, T. Shang, Z.W. Cheng, F. Gao, H. Ishii, K.D. Tsuei, Y.F. Liao, X. Lu, L.H. Tjeng, J.M. Chen, and H.Q. Yuan, *Scientific Reports* **5**, 17608 (2015).
- <sup>50</sup> I. Abbati, L. Braicovich, B. Michelis, A. Fasana, G.L. Olcese, F. Canepa, G.A. Costa, *Sol. St. Comm.* **55**, 1081 (1985).
- <sup>51</sup> S. Doniach and M. Šunjić, *J. Phys. C* **3**, 286 (1970).
- <sup>52</sup> S. Tougaard and P. Sigmund, *Phys. Rev. B* **25**, 4452 (1982).
- <sup>53</sup> O. Gunnarsson and K. Schönhammer, *Phys. Rev. B* **28**, 4315 (1983).
- <sup>54</sup> V.T. Rajan, *Phys. Rev. Lett.* **51**, 308 (1983).
- <sup>55</sup> E.L. Thomas, M.S. Kim, D.A. Sokolov, M.C. Bennett, M.C. Aronson, J.Y. Chan, *J. Sol. St. Chem.* **180**, 2356 (2007).
- <sup>56</sup> U.B. Paramanik, Anupam, U. Burkhardt, R. Prasad, C. Geibel, Z. Hossain, *J. Alloys and Comp.* **580**, 435 (2013).
- <sup>57</sup> H. Yashima, H. Mori, N. Sato, and T. Satoh, *J. Magn. Mater.* **31–34**, 411 (1983).
- <sup>58</sup> K.D. Schotte and U. Schotte *Physics Lett. A* **55**, 38 (1975).
- <sup>59</sup> D.C. Mattis, *The Theory of Magnetism*, Harper & Row, New York, 1965.
- <sup>60</sup> A. Orendáčová, M. Kajňáková, J. Černák, J.-H. Park, E. Čížmár, M. Orendáč, A. Vlček, O.V. Kravchyna, A.G. Anders, A. Feher, and M.W. Meisel, *Chemical Physics* **309**, 115 (2005).

- <sup>61</sup> D.L. Cox and N. Greve, *Z. Phys. B - Condensed Matter* **71**, 321 (1988).
- <sup>62</sup> R. Yu, D. Singh, and H. Krakauer, *Phys. Rev. B* **43**, 6411 (1991).
- <sup>63</sup> Y. Baer, H.R. Ott, J.C. Fuggle, and L.E. De Long, *Phys. Rev. B* **24**, 5384 (1981); J.K. Lang, Y. Baer, and P.A. Cox, *J. Phys. F* **11**, 121 (1981); J.F. Herbst, R.E. Watson, and J.W. Wilkins, *Phys. Rev. B* **17**, 3089 (1978); J.F. Herbst and J.W. Wilkins, *Phys. Rev. Lett.* **43**, 1760 (1979); V.I. Anisimov and O. Gunnarsson, *Phys. Rev. B* **43**, 7570 (1991) and references there in.
- <sup>64</sup> D. Wohlleben, J. Röbler, R. Pott R, G. Neumann, and E. Holland-Moritz, eds. P. Wachter and H. Boppart, *Valence Instabilities* **141**, North-Holland, Amsterdam (1981).
- <sup>65</sup> J. Röbler, *J. Magn. Magn. Mater.* **47-48**, 175 (1985).
- <sup>66</sup> E.E. Vainshtein, S.M. Blokhin, M.N. Bril, I.B. Staryi, and Yu.B. Paderno, *Rus. J. Inorg. Chem.* **10**, 64 (1965).

# Coexistence of magnetic order and valence fluctuations in a Kondo lattice system $\text{Ce}_2\text{Rh}_3\text{Sn}_5$ .

M. Gamża<sup>1,2,3</sup>, R. Gumeniuk<sup>2,4</sup>, U. Burkhardt<sup>2</sup>, W. Schnelle<sup>2</sup>, H. Rosner<sup>2</sup>, A. Leithe-Jasper<sup>2</sup>, and A. Ślebarski<sup>3,5</sup>

<sup>1</sup>*Jeremiah Horrocks Institute for Mathematics, Physics and Astrophysics,  
University of Central Lancashire, Preston PR1 2HE, UK*

<sup>2</sup>*Max-Planck Institute for Chemical Physics of Solids, D-01187 Dresden, Germany*

<sup>3</sup>*Institute of Physics, University of Silesia, 40-007 Katowice, Poland*

<sup>4</sup>*Institute of Experimental Physics, TU Bergakademie Freiberg, 09596 Freiberg, Germany and*

<sup>5</sup>*Centre for Advanced Materials and Smart Structures,  
Polish Academy of Sciences, 50-950 Wrocław, Poland*

(Dated: November 28, 2018)

## I. SUPPLEMENTARY INFORMATION

### A. Metallographic study

The microstructures of the  $\text{Ce}_2\text{Rh}_3\text{Sn}_5$  sample was inspected optically (Zeiss Axioplan 2) and with a scanning electron microscope (Philips XL 30). For the metallographic examination, a piece of about 3 mm diameter was cut from the annealed sample and embedded in conductive resin. Grinding was performed on abrasive papers (500- and 1000-grid silicon carbide). Polishing was done using slurries of 9, 3 and  $1/4 \mu\text{m}$  diamond powder in alcohol-based lubricants.

Images of the sample surface obtained using the optical microscope with polarized light suggest that the sample consists of elongated grains with typical lengths of between  $10 \mu\text{m}$  and  $100 \mu\text{m}$  oriented randomly in various directions (see panels a and b of Fig. 1). Scanning electron microscopy investigations indicate that basically all the grains belong to the  $\text{Ce}_2\text{Rh}_3\text{Sn}_5$  phase. Multiple images recorded from the same sample surface with a secondary electron detector and using a backscattered electron detector with magnifications ranging from  $120\times$  to  $4000\times$  did not detect impurity phases and shown only a uniform sample density.

The chemical composition was investigated by means of wavelength dispersive X-ray spectroscopy (WDXS) using a CAMECA SX100 electron microprobe equipped with a tungsten cathode. The local composition was determined by intensities of the X-ray lines  $\text{CeL}$ ,  $\text{SnL}$  and  $\text{RhL}$  which were excited by an electron beam of 20 nA at 15 keV. The X-rays were focused by large monochromator crystals PET (Pentaerythritol,  $d = 0.437 \text{ nm}$ ) on a gas flow proportional counter. The proportions of the three elements were determined with respect to the appropriate reference materials Rh, Sn and  $\text{CeAl}_2$  and resulted in analytical totals of 100.1(2) wt.% by using the PAP matrix correction model.<sup>1</sup> Measurements on ten points on the sample surface gave the same results within expected experimental error bars (see Table I). After averaging on the ten points, the following contents were obtained: Ce: 20.06(10) at.%, Rh: 29.95(19) at.%, Sn: 49.99(18) at.%. This composition corresponds to  $\text{Ce}_{2.01(1)}\text{Rh}_{3.00(2)}\text{Sn}_{5.00(2)}$  and is in an excellent agree-

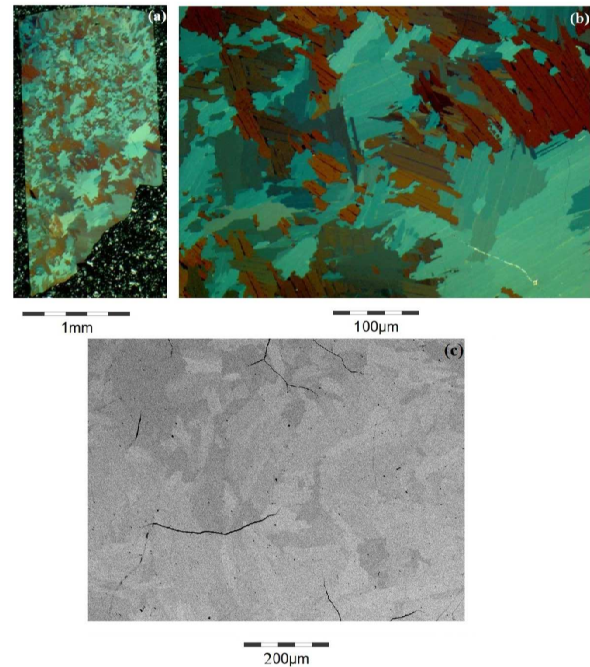


FIG. 1. Metallographic cross-section of an annealed ( $800^\circ\text{C}/14$  days) polycrystalline sample of  $\text{Ce}_2\text{Rh}_3\text{Sn}_5$  showing orientation dependent reflectivity of the grains in optical (polarized light mode, panels a, b) and scanning electron (back scattered electron mode, panel c) micrographs.

ment with stoichiometric  $\text{Ce}_2\text{Rh}_3\text{Sn}_5$ .

### B. X-ray powder diffraction

Phase analysis of the polycrystalline sample was carried out from X-ray powder diffraction patterns collected at room temperature on a HUBER imaging plate Guinier camera G670 using  $\text{Cu } K\alpha_1$  radiation in a  $2\theta$  range of 3–115 degrees with the expose time  $6 \times 15 \text{ min}$ . For powder XRD study, pieces of the sample were converted to a fine powder by grinding in a mortar with a small amount of acetone. Rietveld-type refinement of the powder pattern performed using Jana2006 program<sup>2</sup> gave atomic positional and displacement parameters consistent with re-



TABLE I. Normalized atomic concentrations of Ce, Rh and Sn measured by WDXS method on ten points on the  $\text{Ce}_2\text{Rh}_3\text{Sn}_5$  sample surface.

Nr.	Ce (at.%)	Rh (at.%)	Sn (at.%)
1	20.03	30.26	49.71
2	20.06	29.79	50.14
3	20.10	30.00	49.90
4	20.01	29.81	50.18
5	20.12	30.03	49.86
6	20.08	29.76	50.16
7	19.99	30.15	49.86
8	19.94	29.81	50.25
9	19.95	30.16	49.89
10	20.28	29.77	49.95

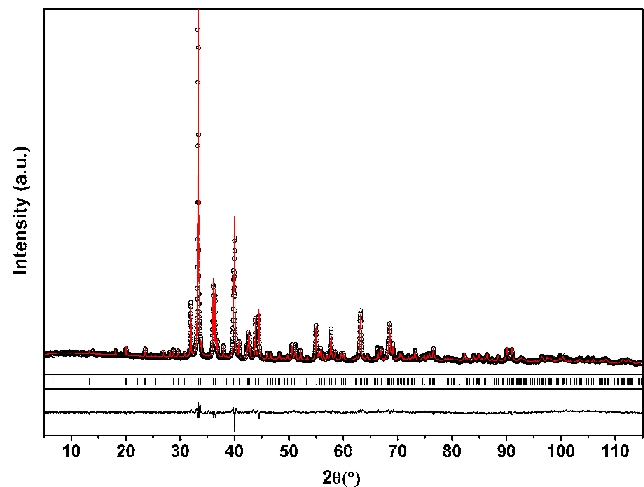


FIG. 2. X-ray powder diffraction pattern for  $\text{Ce}_2\text{Rh}_3\text{Sn}_5$  (black circles) and Rietveld refinement (red lines) that resulted in the following statistical factors:  $R(\text{all}) = 6.92$ ;  $R_w(\text{all}) = 7.25$ ;  $R_p = 5.17$ ;  $R_{wp} = 6.59$ .

sults of our single crystal X-ray diffraction study (see Table II of Ref. 3). Lattice parameters derived from the refinement are:  $a = 4.4992(1)$  Å;  $b = 26.4839(7)$  Å;  $c = 7.2160(2)$  Å. The sample was found to be nearly single phased. Apart from peaks originating from the  $\text{Ce}_2\text{Rh}_3\text{Sn}_5$  phase, there are only few additional very slight features in the diffraction pattern, which we assign to a small amount of an unidentified minority phase (see Fig. 2).

<sup>1</sup> J.L. Pouchou and F. Pichoir, *Rech. Aerosp.* **3**, 13 (1984).

<sup>2</sup> V. Petricek, M. Dusek and L. Palatinus, *Z. Kristallogr.* **229(5)**, 345 (2014).

<sup>3</sup> M. Gamża, R. Gumeniuk, U. Burkhardt, W. Schnelle, H. Rosner, and A. Ślebarski, to be published.